

# A compact, portable device for microscopic magnetic imaging based on diamond quantum sensors

Alex Shaji,<sup>1</sup> Kevin J. Rietwyk,<sup>1</sup> Islay O. Robertson,<sup>1</sup> Philipp Reineck,<sup>1,2</sup> David A. Broadway,<sup>1,\*</sup> and Jean-Philippe Tetienne<sup>1,†</sup>

<sup>1</sup>*School of Science, RMIT University, Melbourne, VIC 3001, Australia*

<sup>2</sup>*ARC Centre of Excellence for Nanoscale BioPhotonics, School of Science, RMIT University, Melbourne, VIC 3001, Australia*

Magnetic imaging based on ensembles of diamond nitrogen-vacancy quantum sensors has emerged as a useful technique for the spatial characterisation of magnetic materials and current distributions. However, demonstrations have so far been restricted to laboratory-based experiments using relatively bulky apparatus and requiring manual handling of the diamond sensing element, hampering broader adoption of the technique. Here we present a simple, compact device that can be deployed outside a laboratory environment and enables robust, simplified operation. It relies on a specially designed sensor head that directly integrates the diamond sensor while incorporating a microwave antenna and all necessary optical components. This integrated sensor head is complemented by a small control unit and a laptop computer that displays the resulting magnetic image. We test the device by imaging a magnetic sample, demonstrating a spatial resolution of  $4\text{ }\mu\text{m}$  over a field of view exceeding  $1\text{ mm}$ , and a best sensitivity of  $45\text{ }\mu\text{T}/\sqrt{\text{Hz}}$  per  $(5\text{ }\mu\text{m})^2$  pixel. Our portable magnetic imaging instrument may find use in situations where taking the sample to be measured to a specialist lab is impractical or undesirable.

Widefield quantum diamond microscopy (QDM), which utilises a layer of nitrogen-vacancy (NV) centres in a diamond chip to image the magnetic fields emanating from a proximal sample, has emerged as a useful technique for quantitative, spatially resolved characterisation of magnetic materials and current distributions [1–3]. Key features of QDM include a large field of view (up to several millimetres), a sub-micron spatial resolution, a high magnetic sensitivity, and operation under ambient conditions. These features have enabled the detection and precise imaging of magnetic signals in a variety of contexts, including magnetic inclusions in rocks [4–6], solid-state ferromagnets [7–12], biological organisms and tissues [13–16], and electric currents in integrated circuits [17–20] and photovoltaic devices [21], to name just a few applications.

One attractive aspect of QDM is its relative simplicity and potential for compactness and low cost. Indeed, there are no moving parts and the primary components required are simply a diamond containing an NV layer, a light source to optically excite the NV layer, a camera to image the red photoluminescence (PL), and a microwave (MW) source to drive the NVs’ spin resonances, allowing optically detected magnetic resonance (ODMR) spectra to be collected and spatially correlated. This makes QDM a promising alternative to established magnetic imaging techniques such as magneto-optical Kerr microscopy, magnetic force microscopy, and Lorentz electron microscopy [22], which are typically costly to own and operate and require a permanent, specialised laboratory space. In contrast, it should be possible to realise a

QDM system sufficiently compact and light-weight to be portable, in the sense that it could be routinely moved by the user according to their needs and space restrictions, and even deployed outside a laboratory environment. This would make applications such as rapid on-site screening of mineral samples or quality control of integrated circuits possible. However, such a portable QDM system has not been demonstrated yet. Furthermore, existing QDM systems are typically cumbersome to operate due to the need to manually place and align the diamond sensor on the sample to be imaged [3], hindering routine use by non-specialists.

In this letter, we report on a QDM device specially designed to be compact, robust, portable, and easy to operate without specialist expertise. Our device assembly relies on a mechanically fixed diamond sensor, thus removing the need for manual handling. All the components necessary for operation are incorporated either in the sensor head or in a small supporting control unit, making the overall system portable. We characterise the performance of our device (field of view, spatial resolution, magnetic sensitivity) and compare two versions differing by the choice of the light source. Future improvements in performance and portability are discussed.

A schematic of the sensor head is presented in Fig. 1(a). It comprises the light source, the camera, an objective lens and other basic optical components (collimation lens, tube lens, dichroic mirror, emission filter), and a permanent magnet used to bias the spin resonances of the NVs. The diamond sensor is attached to the head via a printed circuit board (PCB) equipped with a MW loop antenna to drive the spin resonances. The photographs in Fig. 1(b) show an example realisation of the PCB-diamond assembly, where here a  $4\text{ mm} \times 4\text{ mm} \times 400\text{ }\mu\text{m}$  diamond glued on a supporting glass slide covers a  $4\text{-mm-diameter}$  hole made in the PCB to allow light to go

\* david.broadway@rmit.edu.au

† jean-philippe.tetienne@rmit.edu.au

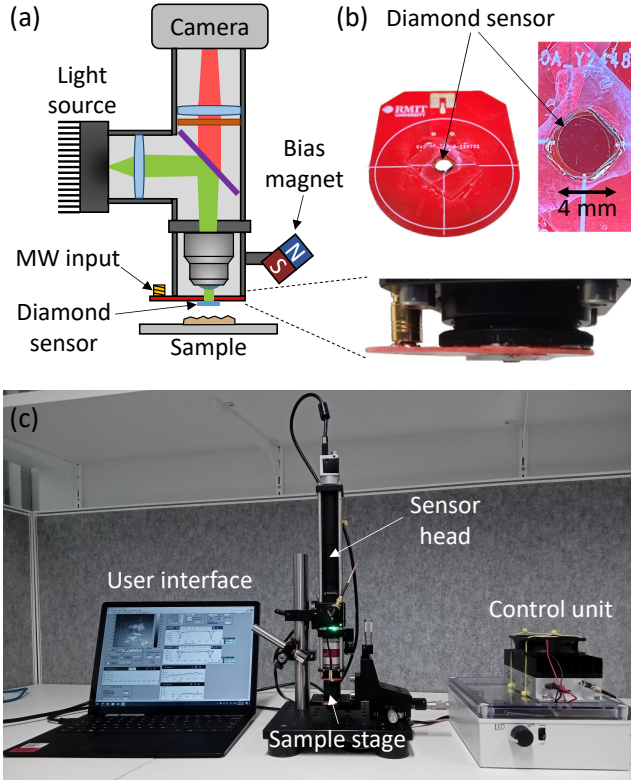


FIG. 1. (a) Schematic of the sensor head of the compact quantum diamond microscope. The magnetically sensitive diamond is placed at the bottom of the head, directly facing the sample to be imaged which is mounted on a separate stage. (b) Photographs of the PCB holding the diamond sensor and integrating a MW loop antenna. (c) Photograph of the complete system, comprising a control unit and a laptop computer.

through, with the MW loop concentric to the hole.

A photograph of the complete setup is shown in Fig. 1(c). The sensor head occupies a volume of  $\sim (10\text{ cm})^3$  and is mounted on a  $20\text{ cm} \times 20\text{ cm}$  breadboard. The sample to be imaged sits on a 3-axis translation stage placed directly under the sensor head, allowing the sample to be brought in contact with the diamond. Apart from the custom PCB and diamond, the sensor head is entirely built from commercially available off-the-shelf components (primarily sourced from Thorlabs) using a cage system. The complete list of components used is given in the Supplementary Material. The control unit [volume  $\sim (20\text{ cm})^3$ ] encloses a MW signal generator (Windfreak SynthNV Pro) and amplifier (Mini-Circuits ZHL-42), a controller for the light source, and a 30 W power supply. The weight of the sensor head (including sample stage and breadboard) and control unit is 4.9 and 2.3 kg, respectively, making the system highly portable. A laptop computer connected to the control unit (to control the MW generator) and the sensor head (to control the camera) runs a custom LabVIEW program serving as the user interface, performing data acquisition and

basic analysis. Advanced data processing to generate a magnetic field image is carried out via a separate Python script.

A critical component of a QDM setup is the green light source, which needs to provide sufficient power density over the desired field of view in order to efficiently excite the NV layer. In the literature this is typically achieved via a high-power ( $\sim 1\text{ W}$ ) diode-pumped solid-state laser, but such lasers tend to be relatively heavy, bulky, and costly, all of which are undesirable features for our portable QDM system. We therefore explored two alternative light sources which can both be directly integrated into the sensor head: a light-emitted diode (LED, Thorlabs M530L4), and a laser diode (LD, Thorlabs L520P50 with mount LDM9T). The collimated light from the chosen light source was passed through a  $f = 50\text{ mm}$  objective lens (Thorlabs TL4X-SAP, 4x, 0.2 NA), which was also used to collect the PL. The LED outputs 460 mW of power, but high emission divergence and finite emitter size limit the maximum power density achievable at the NV layer due to coupling losses (only 160 mW make it to the diamond surface) and a large minimum spot size ( $\sim 2.5\text{ mm}$ ), as illustrated in Fig. 2(a). On the other hand, the LD outputs only 50 mW but can be focused on the NV layer with arbitrary spot size and minimal losses (40 mW at the diamond) [Fig. 2(b)].

To illustrate the pros and cons of each light source, we recorded PL images [Fig. 2(c,d)] of a diamond mounted to the sensor head as shown in Fig. 1(b). The diamonds used in this work are high-pressure high-temperature (HPHT) grown single-crystal substrates in which a 500-nm-thick NV layer was formed at the bottom surface via ion implantation and annealing [23, 24]. Given the pixel size of the camera (Basler acA2040-90um USB3 Mono) and  $f = 150\text{ mm}$  tube lens used, the images are  $3.7\text{ mm} \times 3.7\text{ mm}$  in size. With the collimated LED [Fig. 2(c)], the illumination spot size is  $\approx 2.5\text{ mm}$  as expected (full width at half maximum, FWHM), which allows most of the diamond to be utilised for imaging though this comes at the cost of a relatively low power density ( $\sim 10\text{ W/cm}^2$ ). With the LD [Fig. 2(d)], the desired spot size can be obtained by adjusting the collimation lens, here the spot is elliptical with FWHM of 1.9 and 0.5 mm along its principal axes. Note that the spot could easily be made circular by adding cylindrical lenses. At the centre of the LD spot the power density is more than 3 times larger than in the LED case, as indicated by the PL counts, despite the 4 times lower power. However, a downside of the LD is the poorer clarity of the PL image due to interference effects, contrasting with the much cleaner LED image.

To characterise the spatial resolution of the optical setup, we placed a similar diamond in contact (NV face down) with a metallic marker, providing us with sharp boundaries in the PL image of the NV layer [Fig. 2(e)]. This image was compared with a reflection image of a metallic marker on a glass slide, without the diamond present [Fig. 2(f)]. Line profiles across boundaries [see

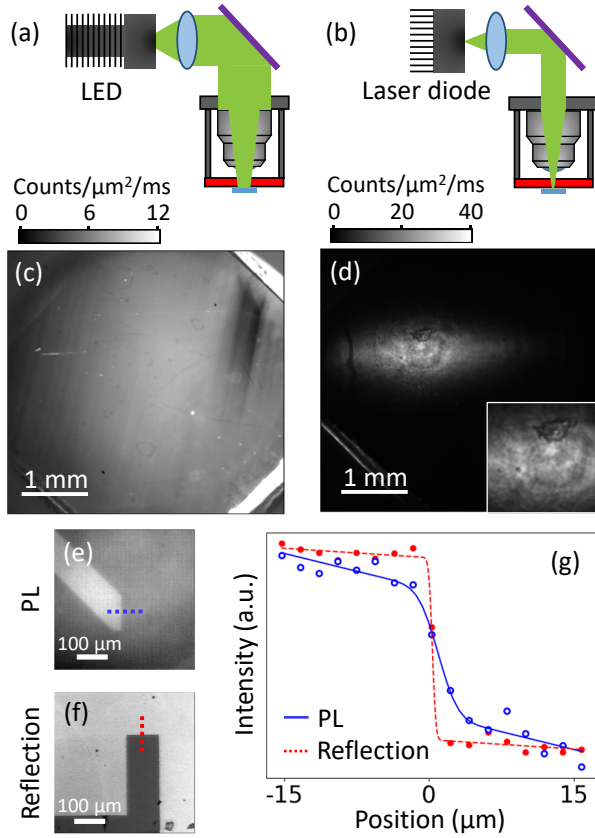


FIG. 2. (a,b) Schematics of the sensor head equipped with either (a) a light emitting diode (LED) or (b) a laser diode as the light source. (c,d) PL images of the NV layer using (c) the LED and (d) the laser diode. The inset in (d) is a magnified view of the centre of the laser spot (1 mm  $\times$  1 mm). (e) PL image of an NV layer in contact with a metallic marker, used to estimate the optical resolution under QDM imaging conditions. (f) Reflection image (using a blue LED at 455 nm wavelength) of a metallic marker on a glass slide, used to estimate the raw optical resolution of the system (i.e., without diamond). (g) Line profiles extracted from (e) and (f) taken along the dotted lines. The two curves are independently rescaled along the  $y$ -axis to facilitate comparison.

examples in Fig. 2(g)] were fitted with an error function, i.e. the convolution of a step function with a Gaussian distribution. The FWHM of the Gaussian is thus a measure of the spatial resolution. In the reflection image, the FWHM is  $1.6 \pm 0.9 \mu\text{m}$ , consistent with the diffraction limit. In the NV PL image, however, it is found to be  $3.9 \pm 1.2 \mu\text{m}$ , larger than the diffraction limit ( $\approx 1.8 \mu\text{m}$  with the objective used at 700 nm wavelength), which is attributed due to the finite NV layer thickness as well as additional diamond-related optical aberrations [25]. This FWHM of about  $4 \mu\text{m}$  thus corresponds to the optical resolution of the system in QDM imaging conditions.

We now test the ability of our portable QDM system to perform magnetic imaging. As a test sample, we used a perpendicularly magnetised CoFeB film (1 nm thick) patterned on a Si substrate, pictured in Fig. 3(a). The sam-

ple was placed on a rubber foot (Thorlabs AV4) sitting on the translation stage, and brought up until full contact with the diamond was achieved [Fig. 3(b)]. The PL image of the NV layer obtained with the LED is shown in Fig. 3(c), in which sample features are clearly visible. We note that the optical focus was fine-tuned after contact with the sample was made, by adjusting the vertical translation stage on which the objective is mounted (Thorlabs SM1ZA), which moves the objective relative to the diamond. When the LD is used instead of the LED, the PL image becomes dominated by interference effects and other illumination inhomogeneities [Fig. 3(d)], making it much harder to locate the region of interest in the sample.

Continuous-wave ODMR spectra were acquired by collecting PL images while sweeping the MW frequency. A small bias magnetic field  $B_0 \approx 8 \text{ mT}$  was applied along one NV orientation family of the (100)-oriented diamond. This allows us to isolate the two spin resonances (at frequencies  $f_{\pm}$ ) of this family in the ODMR spectrum, as shown in Fig. 3(e), here corresponding to the PL from the entire region imaged in Fig. 3(c,d). The typical exposure time per MW frequency was 80 ms (chosen to approach camera saturation) and a MW-off reference frame was taken between each frequency step for normalisation, resulting in a sweep time of less than a minute. Sweeps were repeated to accumulate signal until the desired signal-to-noise ratio was reached. As seen in Fig. 3(e), the ODMR contrast is roughly 3 times higher with the LD ( $\approx 1.2\%$ ) compared to the LED ( $\approx 0.4\%$ ), which is due to the larger excitation power density in the LD case.

A magnetic field map is obtained by fitting the ODMR spectrum to extract the frequencies  $f_{\pm}$  at each pixel and converting to a magnetic field  $B_{\text{NV}} = (f_{+} - f_{-})/2\gamma_e$ . Here  $\gamma_e = 28 \text{ MHz/mT}$  is the electron gyromagnetic ratio and  $B_{\text{NV}}$  is the magnetic field projection along the selected NV axis [3]. The resulting  $B_{\text{NV}}$  maps obtained after fourteen hours of integration are shown in Fig. 3(f,g) for the LED and LD cases, respectively. The characteristic stray field from the perpendicularly magnetised structures is clearly resolved in both cases, but the noise level is significantly lower with the LD. The magnetic sensitivity deduced from the pixel-to-pixel noise in these images is  $224$  and  $45 \mu\text{T}/\sqrt{\text{Hz}}$  with the LED and LD, respectively, per  $(5 \mu\text{m})^2$  pixel (chosen to roughly match the optical resolution). These values can be compared with the theoretical sensitivity in the photon shot noise limit, given by [26]

$$\eta_B = \frac{4}{3\sqrt{3}\gamma_e} \frac{\Delta\nu}{C\sqrt{\mathcal{R}}} \quad (1)$$

where  $\Delta\nu$  is the ODMR linewidth (FWHM),  $C$  the ODMR contrast, and  $\mathcal{R}$  the average photon detection rate (taking the dead times into account). Using the parameters extracted from the experiments, we find a per-pixel sensitivity of  $\eta_B \approx 192$  and  $34 \mu\text{T}/\sqrt{\text{Hz}}$  with the LED and LD, respectively, reasonably close to the actual sensitivity observed indicating the measurement

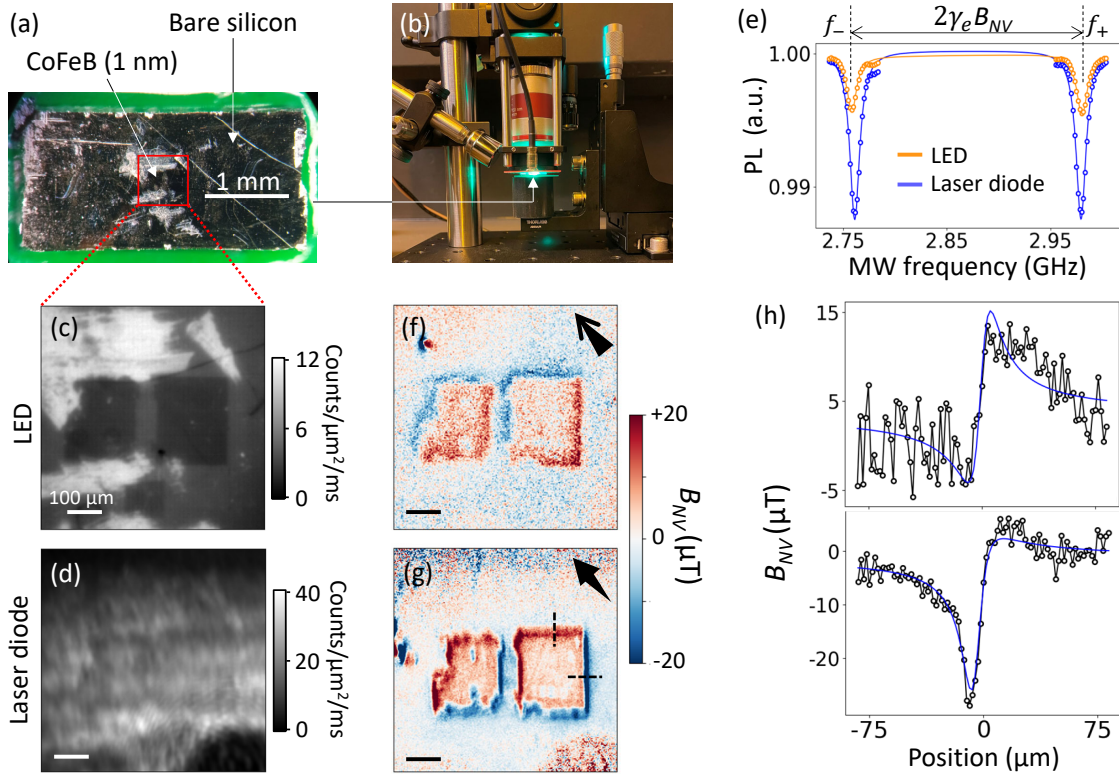


FIG. 3. (a) Photograph of the magnetic test sample. (b) Photograph of the system during data acquisition. (c,d) PL images of the NV layer with the sample in contact, using (c) the LED or (d) the LD as the excitation source. (e) ODMR spectrum integrated over the entire region imaged in (c,d). The solid lines are double Lorentzian fits. (f,g) Maps of the magnetic field projection  $B_{NV}$  corresponding to the PL image in (c,d). N.B: the NV projection axis (set by the external magnet) is different in (f) and (g), as indicated by the black arrow in each image. (h) Line profiles along the vertical (top graph) and horizontal (bottom graph) dashed lines in (g). The solid lines are a fit to a model (see text).

is shot-noise limited (the discrepancy is attributed to the non-optimal sampling of the ODMR spectrum). We note that the measurements reported in Fig. 3 were taken with the system sitting on a regular desk with normal ambient lighting, as pictured in Fig. 1(c).

From these comparative tests we conclude that the LD significantly outperforms the LED in this instance. This is because of the small field of view required to image our test sample [ $\sim (500\mu\text{m})^2$ ] allowing the LD spot size to be optimised accordingly to maximise the power density and hence the sensitivity. Nevertheless, the LED is a suitable option when fields of view at or larger than its minimum spot size ( $\sim 2.5\text{ mm}$  here) are required. A dual illumination system could also be easily incorporated in the sensing head, e.g. LD for NV excitation and LED to facilitate sample positioning.

The magnetic sensitivity could be improved in several ways, as informed by Eq. 1. First, NV layers formed by optimal nitrogen doping during chemical vapour deposition growth typically yield a more favourable  $\Delta\nu/\sqrt{\mathcal{R}}$  ratio than for the HPHT diamond used here [24, 27]. Second, the thickness of the NV layer should be increased to boost  $\mathcal{R}$  so long as the spatial resolution does not become degraded as a result [3]. For instance, here we could have

used a  $2\text{-}\mu\text{m}$ -thick NV layer instead of the  $500\text{-nm}$  layer. Lastly,  $\mathcal{C}$  can be increased further (e.g. to about 3% with the diamond used) using a higher excitation power density ( $\gtrsim 100\text{ W/cm}^2$ ). This will require a higher power laser if the field of view is to be preserved. With the above improvements combined, a per-pixel sensitivity well below  $1\mu\text{T}/\sqrt{\text{Hz}}$  should be achievable (translating into a shorter acquisition time to reach a similar noise level), with modest impact on the portability of the system.

The spatial resolution in the magnetic images results from a convolution between the optical resolution ( $3.9\mu\text{m}$  in the current conditions, as determined above) and the effect of the finite standoff  $d$  between the sample and the NV sensing layer [28]. By fitting a pair of line profiles across perpendicular edges of the magnetic film [Fig. 3(h)] using the model described in Refs. [28, 29], we deduce a standoff of  $d \approx 6.6 \pm 1.2\mu\text{m}$ . This indicates that the magnetic resolution is here dominated by the stand-off effect rather than the optical resolution. Minimising the relative angle between sample and diamond using a goniometric stage was shown to improve standoff, with  $d \approx 1.6\mu\text{m}$  achieved in Ref. [28], and could be incorporated in our system. Simple procedures to clean the diamond surface after each use of the sensing head will



also need to be developed. In addition, the optical resolution could be improved by reducing aberrations, e.g. using a thinner diamond [25]. With these improvements, magnetic images with a  $2\ \mu\text{m}$  resolution should be readily attainable in routine with a portable QDM system.

Finally, we note that the size, weight and power footprint of our current system could be reduced further, especially the control unit where a lower-power MW amplifier could be employed (e.g. Mini-Circuits ZRL-3500). The lower output MW power could be offset by a MW loop antenna with a smaller diameter, though at the cost of a reduced maximum field of view.

In conclusion, we demonstrated a compact and portable version of a quantum diamond microscope, capable of quantitative magnetic field imaging outside a laboratory environment. The performance of our current system was characterised, and future improvements were outlined. Our device may find use in situations where taking the sample to be measured to a specialist lab is impractical or undesirable, for instance for rapid screening of rock samples in the field.

## SUPPLEMENTARY MATERIAL

See supplementary material for additional diamond sample details, additional photographs of the setup, and

a full list of components.

## ACKNOWLEDGMENTS

The authors thank S.C. Scholten for assistance with ODMR data processing and A.J. Healey with diamond cleaning. I.O.R. is supported by an Australian Government Research Training Program Scholarship. This work was supported by the Australian Research Council (ARC) through grants FT200100073, DP220100178 and DE230100192. P.R. acknowledges support through an RMIT University Vice-Chancellor's Research Fellowship.

## DATA AVAILABILITY STATEMENT

The data that supports the findings of this study are available within the article and its supplementary material.

## AUTHOR DECLARATIONS

The authors have no conflicts to disclose.

- 
- [1] S. Steinert, F. Dolde, P. Neumann, A. Aird, B. Naydenov, G. Balasubramanian, F. Jelezko, and J. Wrachtrup, High sensitivity magnetic imaging using an array of spins in diamond, *Review of Scientific Instruments* **81**, 043705 (2010).
  - [2] E. V. Levine, M. J. Turner, P. Kehayias, C. A. Hart, N. Langellier, R. Trubko, D. R. Glenn, R. R. Fu, and R. L. Walsworth, Principles and techniques of the quantum diamond microscope, *Nanophotonics* **8**, 1945–1973 (2019).
  - [3] S. Scholten, A. Healey, I. Robertson, G. Abrahams, D. Broadway, and J.-P. Tetienne, Widefield quantum microscopy with nitrogen-vacancy centers in diamond: Strengths, limitations, and prospects, *Journal of Applied Physics* **130**, 150902 (2021).
  - [4] D. R. Glenn, R. R. Fu, P. Kehayias, D. L. Sage, E. A. Lima, B. P. Weiss, and R. L. Walsworth, Micrometer-scale magnetic imaging of geological samples using a quantum diamond microscope, *Geochem. Geophys. Geosystems* **18**, 3254 (2017).
  - [5] R. R. Fu, E. A. Lima, M. W. R. Volk, and R. Trubko, High-sensitivity moment magnetometry with the quantum diamond microscope, *Geochemistry, Geophysics, Geosystems* **21**, e2020GC009147 (2020).
  - [6] S. C. Steele, R. R. Fu, M. W. R. Volk, T. L. North, A. R. Brenner, A. R. Muxworthy, G. S. Collins, and T. M. Davison, Paleomagnetic evidence for a long-lived, potentially reversing martian dynamo at 3.9 Ga, *Science Advances* **9**, eade9071 (2023).
  - [7] L. Toraille, K. Aïzel, É. Balloul, C. Vicario, C. Monzel, M. Coppey, E. Secret, J.-M. Siaugue, J. Sampaio, S. Rohart, N. Vernier, L. Bonnemay, T. Debuisschert, L. Rondin, J.-F. Roch, and M. Dahan, Optical magnetometry of single biocompatible micromagnets for quantitative magnetogenetic and magnetomechanical assays, *Nano Lett.* **18**, 7635 (2018).
  - [8] D. A. Broadway, S. C. Scholten, C. Tan, N. Dontschuk, S. E. Lillie, B. C. Johnson, G. Zheng, Z. Wang, A. R. Oganov, S. Tian, C. Li, H. Lei, L. Wang, L. C. L. Hollenberg, and J.-P. Tetienne, Imaging domain reversal in an ultrathin van der waals ferromagnet, *Advanced Materials* **32**, 2003314 (2020).
  - [9] I. Meirzada, N. Sukenik, G. Haim, S. Yochelis, L. T. Baczewski, Y. Paltiel, and N. Bar-Gill, Long-time-scale magnetization ordering induced by an adsorbed chiral monolayer on ferromagnets, *ACS Nano* **15**, 5574 (2021).
  - [10] M. Huang, Z. Sun, G. Yan, H. Xie, N. Agarwal, G. Ye, S. H. Sung, H. Lu, J. Zhou, S. Yan, *et al.*, Revealing intrinsic domains and fluctuations of moiré magnetism by a wide-field quantum microscope, *Nature Communications* **14**, 5259 (2023).
  - [11] H. Chen, S. Asif, M. Whalen, J. Támara-Isaza, B. Luetke, Y. Wang, X. Wang, M. Ayako, S. Lamsal, A. F. May, M. A. McGuire, C. Chakraborty, J. Q. Xiao, and M. J. H. Ku, Revealing room temperature ferromagnetism in exfoliated Fe<sub>5</sub>GeTe<sub>2</sub> flakes with quantum magnetic imaging, *2D Materials* **9**, 025017 (2022).
  - [12] S. Lamichhane, K. A. McElveen, A. Erickson, I. Fescenko, S. Sun, R. Timalisina, Y. Guo, S.-H. Liou, R. Y.

- Lai, and A. Laraoui, Nitrogen-vacancy magnetometry of individual fe-triazole spin crossover nanorods, *ACS Nano* **17**, 8694 (2023).
- [13] D. Le Sage, K. Arai, D. R. Glenn, S. J. DeVience, L. M. Pham, L. Rahn-Lee, M. D. Lukin, A. Yacoby, A. Komeili, and R. L. Walsworth, Optical magnetic imaging of living cells, *Nature* **496**, 486 (2013).
- [14] I. Fescenko, A. Laraoui, J. Smits, N. Mosavian, P. Kehayias, J. Seto, L. Bougas, A. Jarmola, and V. M. Acosta, Diamond magnetic microscopy of malarial hemozoin nanocrystals, *Phys. Rev. Appl.* **11**, 034029 (2019).
- [15] J. M. McCoey, M. Matsuoka, R. W. de Gille, L. T. Hall, J. A. Shaw, J.-P. Tetienne, D. Kisailus, L. C. L. Hollenberg, and D. A. Simpson, Quantum magnetic imaging of iron biomineralization in teeth of the chiton *acanthopleura hirtosa*, *Small Methods* **4**, 1900754 (2020).
- [16] S. Chen, W. Li, X. Zheng, P. Yu, P. Wang, Z. Sun, Y. Xu, D. Jiao, X. Ye, M. Cai, M. Shen, M. Wang, Q. Zhang, F. Kong, Y. Wang, J. He, H. Wei, F. Shi, and J. Du, Immunomagnetic microscopy of tumor tissues using quantum sensors in diamond, *Proceedings of the National Academy of Sciences* **119**, e2118876119 (2022).
- [17] M. J. Turner, N. Langellier, R. Bainbridge, D. Walters, S. Meesala, T. M. Babinec, P. Kehayias, A. Yacoby, E. Hu, M. Lončar, R. L. Walsworth, and E. V. Levine, Magnetic field fingerprinting of integrated-circuit activity with a quantum diamond microscope, *Phys. Rev. Appl.* **14**, 014097 (2020).
- [18] P. Kehayias, J. Walraven, A. Rodarte, and A. Mounce, High-resolution short-circuit fault localization in a multilayer integrated circuit using a quantum diamond microscope, *Phys. Rev. Appl.* **20**, 014036 (2023).
- [19] M. Garsi, R. Stöhr, A. Denisenko, F. Shagieva, N. Trautmann, U. Vogl, B. Sene, F. Kaiser, A. Zappe, R. Reuter, and J. Wrachtrup, Three-dimensional imaging of integrated-circuit activity using quantum defects in diamond, *Phys. Rev. Appl.* **21**, 014055 (2024).
- [20] H. F. Wen, Y. Liu, W. Hao, Z. Fu, Z. Gao, D. Wang, X. Li, Z. Li, H. Guo, Z. Ma, Y. J. Li, J. Tang, and J. Liu, Imaging electromagnetic boundary of microdevice using a wide field quantum microscope, *Opt. Express* **32**, 10829 (2024).
- [21] S. Scholten, G. Abrahams, B. Johnson, A. Healey, I. Robertson, D. Simpson, A. Stacey, S. Onoda, T. Ohshima, T. Kho, J. Ibarra Michel, J. Bullock, L. Hollenberg, and J.-P. Tetienne, Imaging current paths in silicon photovoltaic devices with a quantum diamond microscope, *Phys. Rev. Appl.* **18**, 014041 (2022).
- [22] M. R. Freeman and B. C. Choi, Advances in magnetic microscopy, *Science* **294**, 1484 (2001).
- [23] Z. Huang, W.-D. Li, C. Santori, V. M. Acosta, A. Faraon, T. Ishikawa, W. Wu, D. Winston, R. S. Williams, and R. G. Beausoleil, Diamond nitrogen-vacancy centers created by scanning focused helium ion beam and annealing, *Applied Physics Letters* **103**, 081906 (2013).
- [24] A. J. Healey, A. Stacey, B. C. Johnson, D. A. Broadway, T. Teraji, D. A. Simpson, J.-P. Tetienne, and L. C. L. Hollenberg, Comparison of different methods of nitrogen-vacancy layer formation in diamond for wide-field quantum microscopy, *Phys. Rev. Mater.* **4**, 104605 (2020).
- [25] S. Nishimura, M. Tsukamoto, K. Sasaki, and K. Kobayashi, Investigations of optical aberration on quantum diamond microscopy toward high spatial resolution and sensitivity, Preprint **arXiv:2402.14422** (2024).
- [26] J. F. Barry, J. M. Schloss, E. Bauch, M. J. Turner, C. A. Hart, L. M. Pham, and R. L. Walsworth, Sensitivity optimization for nv-diamond magnetometry, *Rev. Mod. Phys.* **92**, 015004 (2020).
- [27] E. E. Kleinsasser, M. M. Stanfield, J. K. Q. Banks, Z. Zhu, W.-D. Li, V. M. Acosta, H. Watanabe, K. M. Itoh, and K.-M. C. Fu, High density nitrogen-vacancy sensing surface created via He+ ion implantation of 12C diamond, *Applied Physics Letters* **108**, 202401 (2016).
- [28] G. J. Abrahams, S. C. Scholten, A. J. Healey, I. O. Robertson, N. Donschuk, S. Q. Lim, B. C. Johnson, D. A. Simpson, L. C. L. Hollenberg, and J.-P. Tetienne, An integrated widefield probe for practical diamond nitrogen-vacancy microscopy, *Applied Physics Letters* **119**, 254002 (2021).
- [29] T. Hingant, J.-P. Tetienne, L. J. Martínez, K. Garcia, D. Ravelosona, J.-F. Roch, and V. Jacques, Measuring the magnetic moment density in patterned ultrathin ferromagnets with submicrometer resolution, *Phys. Rev. Appl.* **4**, 014003 (2015).

## Supplementary Material

### I. DIAMOND SENSOR DETAILS

The diamond sensors used in this work were made from  $4\text{ mm} \times 4\text{ mm} \times 400\text{ }\mu\text{m}$  type-Ib, single-crystal diamond substrates grown by high-pressure, high-temperature (HPHT) synthesis, with  $\{100\}$ -oriented polished faces, purchased from Chenguang Machinery & Electric Equipment. To form a dense NV layer near the surface, the diamonds were implanted with 2 MeV Sb ions with a dose of  $2 \times 10^{11}$  ions/cm<sup>2</sup>. Full cascade Stopping and Range of Ions in Matter (SRIM) Monte Carlo simulations indicate that the distribution of created vacancies extend to about 500-600 nm below the surface, with a peak at  $\approx 400$  nm. Following implantation, the diamond was annealed at 900 °C for 4 hours in a vacuum of  $\sim 10^{-5}$  Torr to form the NV centers. After annealing, the plate was acid cleaned (30 minutes in a boiling mixture of sulphuric acid and sodium nitrate).

The same diamond was used throughout the main text except in Fig. 2(e) where a different diamond (though nominally identical) was employed to determine the optical resolution.

### II. SETUP DETAILS

This section provides further details about the device presented in the main text, with the aim of facilitating replication.

The inside of the control unit is shown in Fig. S1, and the components listed in Table I. The typical retail price of each component is also indicated. A MW isolator is included to protect the amplifier. A 30 W, 15 V AC/DC converter supplies power to the amplifier, fan, and LED controller. For the laser diode version (not shown), the LED Controller is replaced with the laser driver (listed in Table III) and an appropriate AC/DC converter is added. Not shown in the photograph in Fig. S1 (but visible in Fig. 1(c) of the main text) is the microwave (MW) amplifier which is placed on the lid of the enclosing box, and the fan attached to the amplifier to prevent overheating.

Photographs of the microscopy setup (sensor head and sample stage on breadboard) are shown in Fig. S2, taken from a different viewpoint to Fig. 1(c) of the main text to better show the light source. Fig. S2(a) and S2(b) show the version with the LED and laser diode, respectively. The components are listed in Table II, except for the components specific to each light source which are listed separately in Table III.

As mentioned in the main text, the only element that is not commercially available is the custom printed circuit board (PCB) holding the diamond. To connect the PCB to the optical system, a Thorlabs internal locking ring (SM1NT) was glued to the PCB and coupled to a lens tube through an external thread adapter (SM1T2).

The total approximate cost of the entire system is indicated in Table III for the two versions, not including the cost of the diamond sensor, custom PCB, laptop, and software.

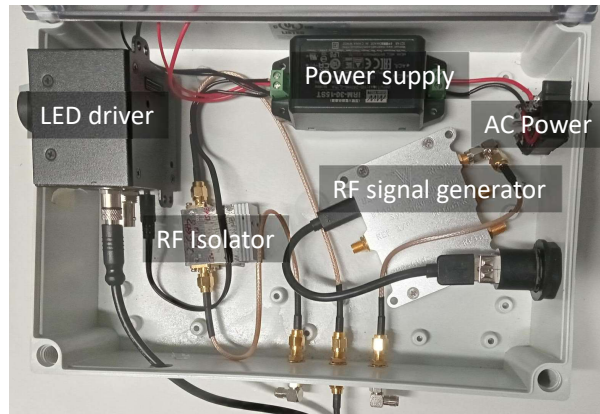


FIG. S1. Photograph showing the components inside the control unit, for the LED version.

Description	Item reference	Price (US\$)
Plastic box	Bud Industries, PIP-11775-C	55.69
MW signal generator	Windfreak, SynthNV Pro	1,199.00
MW amplifier	Mini-Circuits, ZHL-42+	1,132.18
MW isolator	UIY, UIYBCI3038A2T6SF	360.00
Fan for amplifier	Sanyo Denki, 109R0824G4021	51.17
AC/DC converter	Mean Well, IRM-30-15ST	19.49
AC power connector	TE Connectivity, 1609112-3	18.31
LED controller power cable	Tensility International Corp, CA-2193	4.14
USB C to USB A connector	Adafruit Industries, 4259	9.47
USB A to USB C cable	Adafruit Industries, 4472	4.69
SMA to SMA connectors	Cinch Connectivity, 142-0901-401 (3x)	55.14
SMA to SMA coaxial cables	Cinch Connectivity, 415-0029-MM500 (5x)	86.35
	Cinch Connectivity, 415-0029-036	19.01
SMA 'L' connectors	TE Connectivity Linx, CONSMA010 (5x)	26.50
SMA to SMB coaxial cable	Taoglas Limited, CAB.0101	7.90
<b>Total</b>		<b>3,049.04</b>

TABLE I. List of components contained in the control unit (excluding light source controller, which is listed in Table III), and their typical retail price.

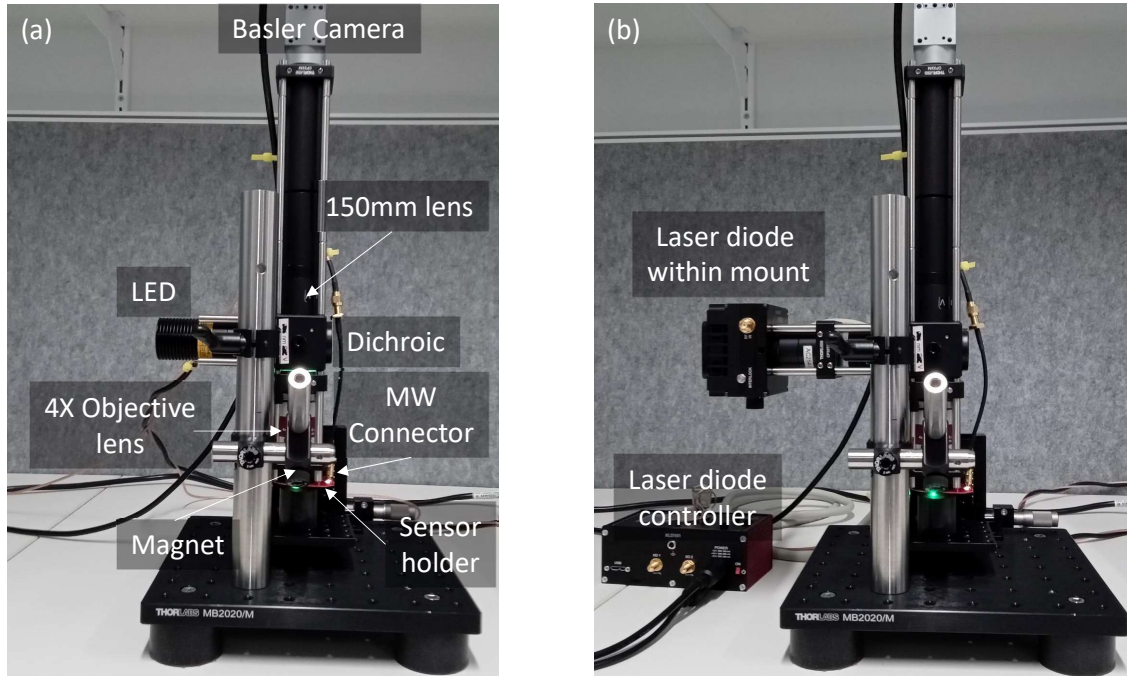


FIG. S2. (a,b) Photograph showing the system with (a) LED and (b) laser diode, as the excitation source.



Description	Item reference	Price (US\$)
Camera	Basler, acA2040-90um Mono USB 3.0	1,430.00
Dichroic beam splitter (640 nm LP)	Semrock, FF640-FDi01-25x36	390.00
Cage cube mount for dichroic	Thorlabs, CM1-DCH	192.44
Z-axis translation mount for objective	Thorlabs, SM1ZA	220.20
Objective lens	Thorlabs, TL4X-SAP	2,308.01
Cage plates	Thorlabs, CP33T + CP36 + CP4S-SM1	72.23
Filters (600 nm SP + 650 nm LP)	Thorlabs, FESH0600 + FELH0650	287.62
Tube lens $f = 150$ mm	Thorlabs, AC254-150-B	103.65
Cage construction rods	Thorlabs, ER4 (4x) + ER3 (4x) + ER2 (8x) + ER1 (4x)	132.32
Lens tubes for optics	Thorlabs, SM1L30 + SM1L20 + SM1L10 (2x) + SM1L05 (3x) + SM1L03	131.89
Adapters for PCB	Thorlabs, SM1NT + SM1T2	31.23
SMB-PCB connector	JAE Electronics, SMBR004D00	3.00
Neodymium magnet	AMF Magnetics, AMFYPC16 (threaded pot) + D-D18H15-N48 (disc)	16.03
Construction posts	Thorlabs, RS100P4 + RS150P4 + TR75 (2x)	77.26
Clamp to hold cage	Thorlabs, CH1030	96.15
Right angle clamps for magnet	Thorlabs, RA90 + RA90RS	42.01
Breadboard + rubber feet	Thorlabs, MB2020 + AV4 (4x) + AV3 (for sample)	214.39
XYZ translation stage for sample	Newport, M-460A-XYZ	884.00
Right angle bracket for sample stage	Thorlabs, AB90A	30.58
Plate for sample	Thorlabs, RB13P1	60.59
<b>Total</b>		<b>6,723.60</b>

TABLE II. List of components making up the microscopy setup (excluding light source, which is listed in Table III).

Description (LED version)	Item reference	Price (US\$)
Mounted LED	Thorlabs, M530L4	325.49
LED driver	Thorlabs, LEDD1B	355.18
Collimating lens $f = 20$ mm	Thorlabs, ACL2520U-A	33.85
<b>Total</b>		<b>714.52</b>
<b>Final total (inc. all components)</b>		<b>10,487.16</b>
Description (Laser diode version)	Item reference	Price (US\$)
Laser diode	Thorlabs, L520P50	76.61
Mount with integrated TEC	Thorlabs, LDM9T	937.13
Laser diode driver	Thorlabs, KLD101	973.85
AC/DC power supply	Thorlabs, TPS002	128.29
Collimating lens adapter	Thorlabs, S1TM12	26.73
Collimating lens $f = 8$ mm	Thorlabs, C240TMD-A	97.49
Widefield lens $f = 75$ mm	Thorlabs, AC254-075-A	89.10
<b>Total</b>		<b>2,329.20</b>
<b>Final total (inc. all components)</b>		<b>12,101.84</b>

TABLE III. List of components specific to the LED or laser diode versions, with the total price of the entire system indicated.